



# Projection micro-stereolithography versus master–slave approach to manufacture a micro-optofluidic device for slug flow detection

Lorena Saitta<sup>1</sup> · Giovanni Celano<sup>1</sup> · Gianluca Cicala<sup>1,2</sup> · Maria Elena Fragalà<sup>2,3</sup> · Giovanna Stella<sup>4</sup> · Matteo Barcellona<sup>3</sup> · Claudio Tosto<sup>1</sup> · Maide Bucolo<sup>4</sup>

Received: 2 December 2021 / Accepted: 5 February 2022 / Published online: 16 March 2022  
© The Author(s) 2022, corrected publication 2022

## Abstract

In this work, the use of projection micro-stereolithography (PμSL) to 3D print a micro-optofluidic device for slug flow detection is presented. For comparison purposes, a poly-dimethylsiloxane (PDMS)–based device was also manufactured by a novel master–slave 3D printing approach. The micro-optofluidic device has a microfluidic T-junction with a micro-optical section that consists of two optical fiber insertions used for slug flow detection. The design of the device also includes two micro-channels for the optical fiber’s insertion, needed to acquire a light signal, which give a direct information about the microfluidic channel inner flow by exploiting the absorption phenomenon. The working principle in the detection is based on a different light transmission correlated to the fluid interfering with the laser beam in a micro-channel section. The two materials used for the two manufacturing approaches were fully characterized in terms of their surface properties via both Atomic Force Microscopy (AFM) and angle of contact measure.

The process within the two micro-channels was monitored optically and a signal correlated to the slug passage was analyzed for the flow tracking. A wide experimental campaign was done for the device manufactured through the PμSL technique in different operative conditions. Thus, the optimal one was identified through the Analysis of Variance (ANOVA). Then, a detailed comparison between the slug process detected inside the HTL resin device and the PDMS device was carried out to evaluate the pros and cons of using different materials and fabrication techniques. The analysis run on the two devices revealed that the HTL resin device can be used for slug flow detection, but future research is still needed to obtain a resin allowing to outperform the PDMS device.

**Keywords** 3D printing · Projection micro-stereolithography · Micro-optics · Microfluidics · Real-time monitoring · Slug flow

---

✉ Lorena Saitta  
lorena.saitta@phd.unict.it

Giovanni Celano  
giovanni.celano@unict.it

Gianluca Cicala  
gianluca.cicala@unict.it

Maria Elena Fragalà  
me.fragala@unict.it

Giovanna Stella  
giovanna.stella@phd.unict.it

Matteo Barcellona  
matteo.barcellona@phd.unict.it

Claudio Tosto  
claudio.tosto@unict.it

Maide Bucolo  
maide.bucolo@unict.it

- <sup>1</sup> Department of Civil Engineering and Architecture, University of Catania, Viale Andrea Doria 6, 95125 Catania, Italy
- <sup>2</sup> INSTM-UDR CT, Viale Andrea Doria 6, 95125 Catania, Italy
- <sup>3</sup> Department of Chemical Sciences, University of Catania, Viale Andrea Doria 6, 95125 Catania, Italy
- <sup>4</sup> Department of Electrical Electronic and Computer Science Engineering, University of Catania, Viale Andrea Doria 6, 95125 Catania, Italy

## 1 Introduction

Lab-on-a-chip has gained a significant attention starting from 1990s [1]. In these devices, a micrometric channel allows small volumes of fluids to be tested. Lab-on-a-chip devices can perform many operations usually needed in conventional biochemistry laboratories, from sample preparation to reaction, detection, and other procedures [2, 1]. Moreover, their use is widely spreading thanks to advantages in terms of low-cost in manufacturing; power consumption saving; reduced time of analysis; and mostly a small fluid expenditure for biological, chemistry, and medical applications [3–5, 7, 8]. Within this context, lab-on-a-chip devices are used to detect and control slug flows into micro-channel, both in biomedical fields and chemical processes [5–9]. The term slug flow refers to two immiscible fluids, which can be gas–liquid, immiscible liquid–liquid, or liquid and microparticles, one dispersed in the other, and circulating into the same microsystem [10, 11]. Among the methods present in literature to detect slug flows, the optical one is advantageous in running an ample range of measurements and being minimally invasive [10].

In this study, a portable micro-optofluidic device designed by the authors [12, 13] was manufactured by using two different 3D printing techniques, the first one is the Projection Micro Stereolithography (PμSL) technique using the photocurable HTL resin, while the second one is the master–slave approach using the poly-dimethylsiloxane (PDMS). The slug process inside microchannel was monitored optically to evaluate its stability and the fluid interaction with the used materials. Thanks to the proposed fabrication approaches, it is possible to reduce the fabrication costs and maintain a satisfactory building resolution.

In the past, the microfluidic devices were produced by means of deposition, microfabrication photolithography, and etching processes. The materials used were silicon, quartz, and glass [14–19]. However, many disadvantages were experienced with these approaches as high raw material costs, time-consuming, and expensive processes needing cleanrooms and limited channel geometries. To overcome all these limits, polymers were introduced since they are cheaper than glass or silicon [20], suitable for mass production, and biocompatible. Furthermore, polymers display good gas permeability, which is fundamental for biochemistry applications, together with a satisfying optical transparency, that is essential in microfluidics to implement optical detection methods for observing and extracting information from biological or chemical samples [21–26].

Among all the polymer types tested in the past decade, PDMS has emerged as the preferred choice [27]. PDMS can be easily molded by casting to create micro

and nano-structures with a fabrication process called soft lithography [28]. PDMS has relevant good properties, like nontoxicity, low temperature curing, and transparency down to 280 nm which enable the use for optical detection, good gas permeability, and it is chemically inert. However, some important limitations can be evident in its use. First, once the PDMS device is fabricated, it is possible that the micro-channel walls will undergo surface deformation due to the exposure to non-polar organic solvents. These variations are caused by the swelling phenomena. Second, being the PDMS quite chemically inert, in the manufacture of devices, it does not allow permanent bonding with itself and it is not easy to permanently attach molecules or polymers of a different nature to its surface [1, 29]. This limits the possibility to assemble complex structures because of poor adhesive bonding. Nonetheless, recent progress to alter deliberately PDMS surface and bulk properties is presented in [30] and different strategies to bond PDMS with various rigid and flexible substrate materials are presented in [31]. Third, PDMS softness and thermal expansion make difficult to obtain high dimensional accuracy [28]. From the processing point of view, even if the soft lithography is a low-cost process, it takes a long time to produce a device, since it requires several processing steps for the manufacturing: fabrication of the master mold, PDMS liquid polymer mixing preparation, casting procedure, PDMS curing, and demolding [32].

The proposed novel approaches based on 3D printing technologies and the used materials (PDMS and HTL resin) overcome all these weaknesses to manufacture micro-devices.

The standard master–slave micro-fabrication methods, such as soft lithography and photolithography, traditionally used to fabricate lab-on-a-chip [28, 33] are expensive and time-consuming [34] and in particular suffer from limited availability of compatible biological materials [35]. The most widely used material with these fabrication methods is PDMS, thanks to its biocompatibility and flexibility [30]. The possibility to print a microdevice in one step with PDMS is still under investigation [36]; on this purpose, an ad hoc master–slave fabrication protocol PDMS–based 3D printing was implemented by the authors [12, 13]. The master–slave protocol, nevertheless, needs more steps for fabrication, offers several advantages including the need of simple equipment, the use of low-cost materials, and no strictly controlled environment.

The second proposed 3D printing approach is the vat polymerization technique named PμSL patented by the company BMF ([www.bmf3d.com](http://www.bmf3d.com)) using the photocurable HTL resin. The PμSL shows several advantages: short turn-around time, down to micron precision, and complex shape printing. The HTL resin-based 3D-printed device was

manufactured in one piece (with no assembly between parts) and uses a one-step manufacturing procedure [1, 25, 26]. The authors' proposed method is an alternative to the stereolithography technology, which is recently used to fabricate organ-on-chip for their compatibility with biomaterials [37, 38].

In this work, the two innovative approaches, PDMS-based 3D printing and PμSL 3D printing, open the way to new fabrication strategies in lab-on-a-chip and organ-on-a-chip devices realization. In particular, two micro-optofluidic devices, having the same geometry integrating both micro-optical and microfluidic components, have been designed for slug flow detection in micro-channel. The process was monitored optically and a signal correlated to the slug passage was analyzed for the flow tracking. A wide experimental campaign was done in different operative conditions. The information related to the slug passage, extracted from the signals, was considered to characterize the process within the HTL resin device. The stability of the process was investigated by using a replicated general factorial design. This also allows to identify which is the experimental operative condition for the optimal use of the micro-device. Once the optimal operative condition was selected, a detailed comparison between the slug process detected inside the HTL resin device and the PDMS device was carried out to evaluate the pros and cons of using different materials and fabrication techniques. The two materials used for the device manufacturing, i.e. PDMS and the HTL resin, respectively, were then analyzed in terms of their surface's roughness and water angle contact to fully understand the hydrodynamic differences detected within the two micro-channels.

## 2 Materials and device processing techniques

### 2.1 Materials

The master–slave for PDMS casting was printed using two materials: VeroWhitePlus RGD835 and FullCure705. RGD835 was purchased from OVERMACH S.p.A. (Parma, Italy) and it is a proprietary blend of acrylate monomers and photoactivators. FullCure705 was purchased from OVERMACH S.p.A. (Parma, Italy) and, as for RGD835, it is a proprietary blend of acrylate monomers and photoactivators. FullCure705 is a breakaway support which is removed by water jetting once the printing process is accomplished. The breakaway support is not part of the final device and is only needed to print not supported cavities.

The master–slave was 3D-printed on a 3D Printer Stratasys Objet260 Connex1 (Stratasys, Los Angeles, CA, USA) and it was used as mold to cast the *Device 1*. For casting *Device 1*, the SYLGARDTM 184 Silicone Elastomer kit,

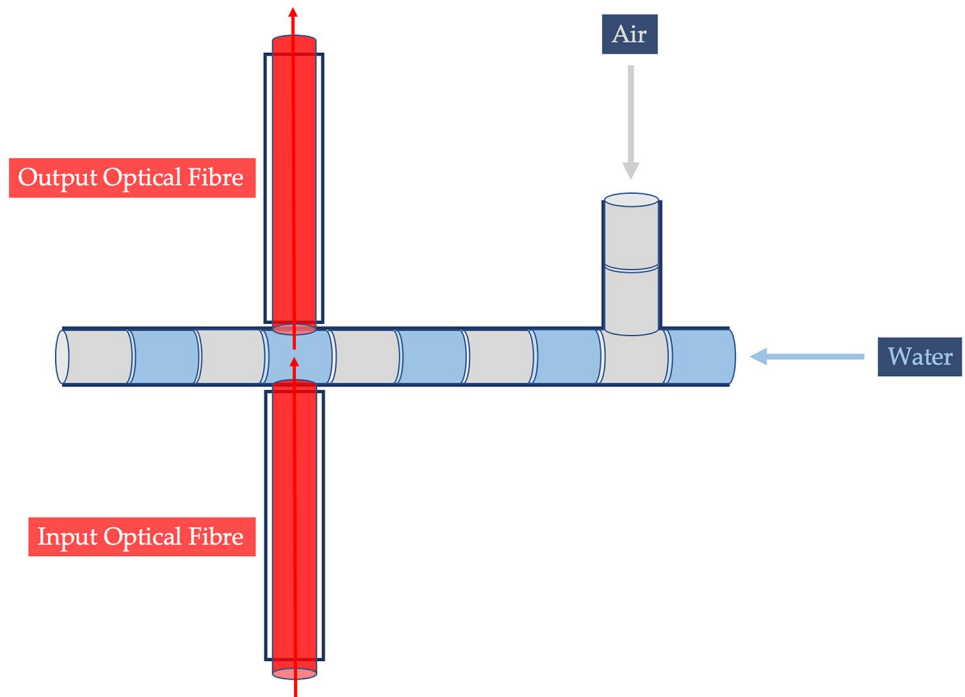
composed by a Polymethyl Siloxane (PDMS) elastomer and a suitable curing agent, was purchased from Farnell Italia S.R.L. (Sylgard 184 elastomer kit, Dow Corning, 148 Midland, Michigan, USA). The procedure used for the manufacturing is detailed elsewhere [39].

HTL resin is a high performance, rigid, and heat-resistant yellow resin proprietary developed by Boston Micro Fabrication (BMF, Maynard, Massachusetts). HTL was used to manufacture the *Device 2* printing on the microArch@S140 ultra-high resolution (10 μm) 3D printer (BMF, Maynard, Massachusetts). This resin grade was selected because of its temperature stability and mechanical properties making it suitable for autoclave sterilization. The resin has, according to its technical data sheet (TDS), a heat distortion temperature (HDT) equal to 140.7 °C (@0.45 MPa) and a Glass Transition Temperature (T<sub>g</sub>) of 172 °C. This last parameter is the temperature at which the amorphous regions experience transition from rigid state to more flexible state making the temperature at the border of the solid state to rubbery state [40]. Therefore, the resin is suitable for repeated autoclave cycles making the device suitable for multiple reuses.

### 2.2 Micro-optofluidic device design and working principle

The micro-optofluidic system that we tested in this work exploits the absorption phenomenon, thus being two different fluids characterized by two different refractive indexes; once an incident laser beam interacts with them, it will be possible to have a different nature of transmission of the light strictly dependent on the fluid with which it is interacting at a precise moment. The working principle is shown in Fig. 1. To practically exploit this physical principle, the geometry of the micro-optofluidic device has been appropriately determined, also thanks to the help of appropriate simulations reported in previous studies [2]. Briefly, the device has two inlets, necessary for the inlet of the two fluids characterizing the two-phase fluid to be studied, which are connected to the two micro-channels that, forming a T-junction, guarantee the formation of the slug flow. At a sufficient distance from the T-junction for the two-phase flow stabilization, with orthogonal orientation to the main microfluidic channel, the micro-channels for the optical fiber's insertion have been designed. From one side of the device, the input optical fiber conveyed the laser light, which by crossing through the center of the microfluidic channel, is then detected by a second optical fiber (the output one), which is aligned with the input one. Using this design, it was possible to acquire a light signal giving direct information about the microfluidic channel inner flow. The flow exits from the main microfluidic channel through an outlet which conveys the fluid to a pressure sensor which can be used as a further detection tool.

**Fig. 1** Working principle of the investigated micro-optofluidic device



The two devices manufactured by the two processing approaches have the same design in terms of micro-channel dimensions, optical section location, inlet and outlet channels dimension, and T-junction geometry. As shown in Fig. 2, all these features characterize the two devices, although some changes have been made to *Device 2* made in HTL resin, in terms of inlets and outlet positioning, compared to *Device 1* made in PDMS [39]. This choice allowed to improve the flow stabilization because of the absence of abrupt direction changes. In fact, even if the inlets and outlet channel's dimension remained unchanged, these are orthogonal to the

microfluidic channel in *Device 1* and, instead, are coaxial and aligned with the main microfluidic channel in *Device 2*. The former design choice for PDMS device is forced by the manufacturing approach that, being based on resin's casting, makes impractical to realize coaxial inlets and outlets.

### 2.3 Micro-optofluidic device fabrication processes

In this study, two devices, which differ from each other for the fabrication process and the raw materials used, were compared. The first micro-optofluidic system (*Device 1*) was

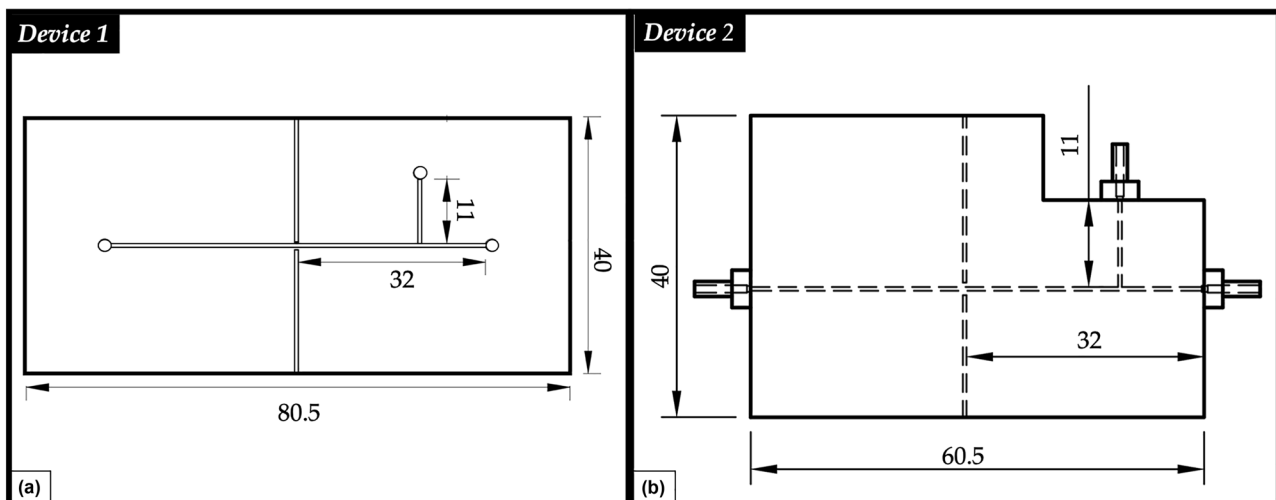


**Fig. 2** Comparison from the top view between **a** *Device 1* (PDMS) and **b** *Device 2* (HTL resin) geometries. Sizes are expressed in mm

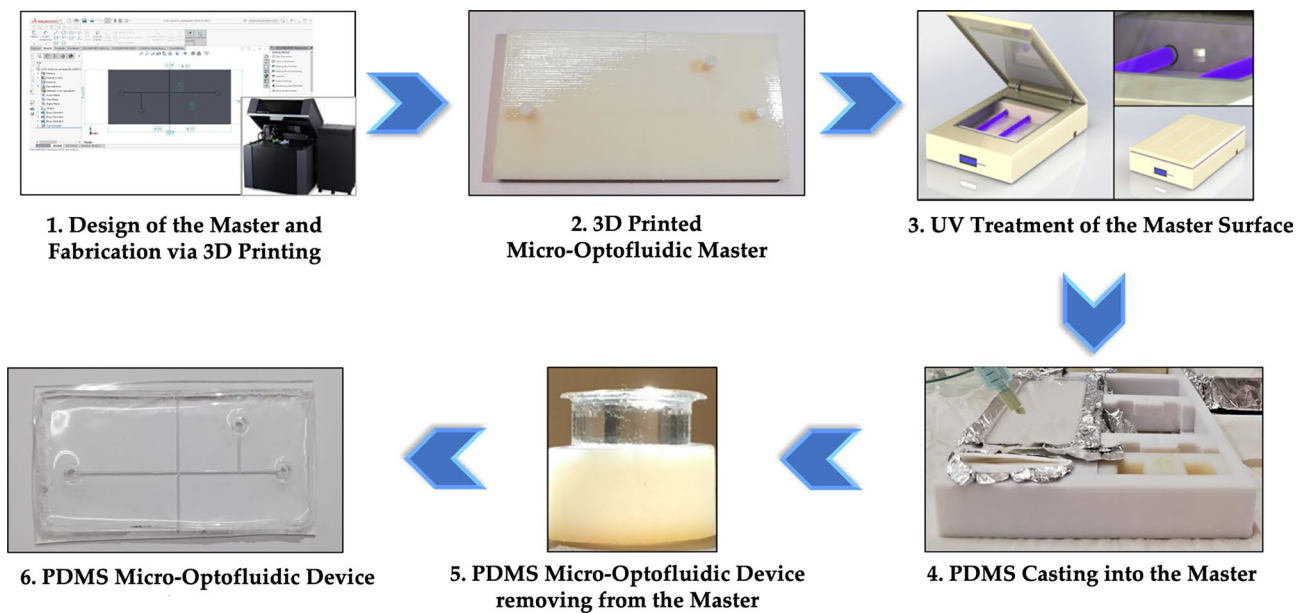


Fig. 3 Procedure followed to fabricate the final *Device 1*

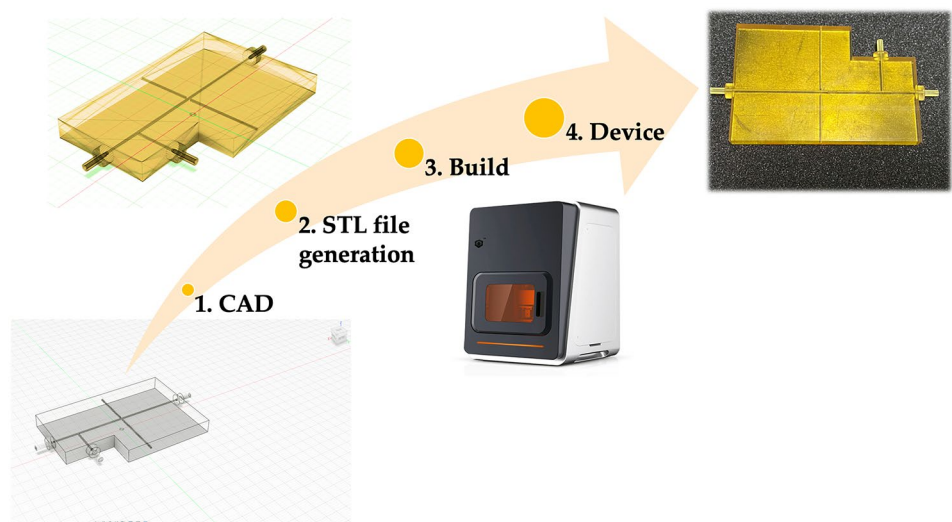
realized using PDMS with a fabrication process which has already been explained elsewhere in detail [27]. The followed fabrication procedure is summarized in Fig. 3.

The *Device 2*, conversely, was directly manufactured by using the P $\mu$ SL technique, which allows for ultra-high resolution, accuracy, and precision. P $\mu$ SL is a hybrid technique combining the benefits of SLA (Stereolithography) and DLP (Digital Light Processing) 3D printing techniques. Basically, micro-sized parts are printed in the top down direction, as it happens in the SLA, but the resin is cured as done in DLP, i.e. by using a digital projection screen rather than a small spot laser.

*Device 2* was designed using Autodesk® Fusion 360 first and then the STL file was transferred to the 3D printer for the build step (Fig. 4). The microArch® S140 ultra-high resolution (10  $\mu$ m) 3D printer was used for the printing.

The *Device 2* being designed and printed as a single piece avoids fluid leakage phenomena or adhesive bonding issues. In addition to that, this processing approach allows to directly integrate the inlets and outlets for fluid flow in the device itself.

Fig. 4 Steps followed to fabricate the final *Device 2* with P $\mu$ SL approach





### 3 Characterization techniques

#### 3.1 Slug flow detection setup

The slug flow through the micro-optofluidic device has been obtained by simultaneously pumping deionized water and air through the two inlets and the T-junction geometry. In fact, the two inlets have been connected to two different syringe pumps (neMESYS low pressure module, Cetoni GmbH, Korbussen, Germany), which have been filled with deionized water and air, respectively. The constant flow rate has been varied at three levels: {0.1, 0.2, 0.3} ml/min.

A laser system (NovaPro 660–125, RGB Lasersystems, Kelheim, Germany) with an emission wavelength equal to 600 nm and an output power ranging between 1 and 3 mW has been used as the light source aimed at detecting the two phases.

Finally, to test the designed micro-optofluidic device, three different measurement systems have been considered:

- A photodiode (PDA100A, Thorlabs, Newton, NJ, USA) with a gain range between 30 and 40 dB, measuring the light intensity variation, connected to a PC oscilloscope (Picoscope 2204A, Pico Technology, Cambridgeshire, UK) with a sampling frequency of 1.5 kHz.
- A digital USB microscope placed above the optical acquisition section that allowed the interactions between the main microfluidic channel and the light transmission to be monitored.
- A pressure sensor (SLF3S-1300F, Sensirion, Stäfa, Switzerland), having a sampling frequency equal to 200 Hz, monitoring the stability of the upstream fluid flow rate externally to the channel.

A block scheme and a real picture of the experimental setup used for the slug flow detection are shown in Fig. 5a and b, respectively.

#### 3.2 The acquired signal and its processing

The acquired signals by the photodiode are a square wave. This behavior is justified by the different refractive index that characterizes the two fluids generating the tested two-phase flow; the refractive indexes for the air and the water are respectively equal to  $n_{Air} = 1.0$  and  $n_{Water} = 1.3$ .

Under these conditions, the higher level of the square wave signal corresponds to the water slug, while the lower level corresponds to the air slug. Each transition from the high to the low level of the square wave is characterized by the presence of signal peaks depending on the transitory phase between the two fluid fronts. The signal detected by the photodiode is shown in Fig. 6.

The optical signals need signal smoothing. The signal post-processing was carried out using a Matlab (Math-Works®) routine as described elsewhere in detail [28]. After the acquisition phase, a low-pass filter with a 40 Hz cut-off frequency has been applied to saturate the signals, thus eliminating high frequency components. Then, a smoothing procedure has been run to generate perfect square wave signals. By overlying the square wave to the saturated signals, it has been possible to identify the time frames corresponding to the air detection ( $T_a$ ), and the time frames corresponding to the water detection ( $T_w$ ) by the device.

In addition, to evaluate the mean period associated to a complete air–water slug passage, the optical signal has been analyzed in the frequency domain. In fact, by obtaining the frequency spectrum, at first it was possible to determine the frequency peak ( $f_{ph}$ ), and then it was possible to determine the mean period  $T_{ph}$  by calculating the reciprocal of this parameter.

#### 3.3 Surface characterization techniques

Two surface characterization techniques were used: Atomic Force Microscopy (AFM, NTEGRA, NT-MDT, Zelenograd,

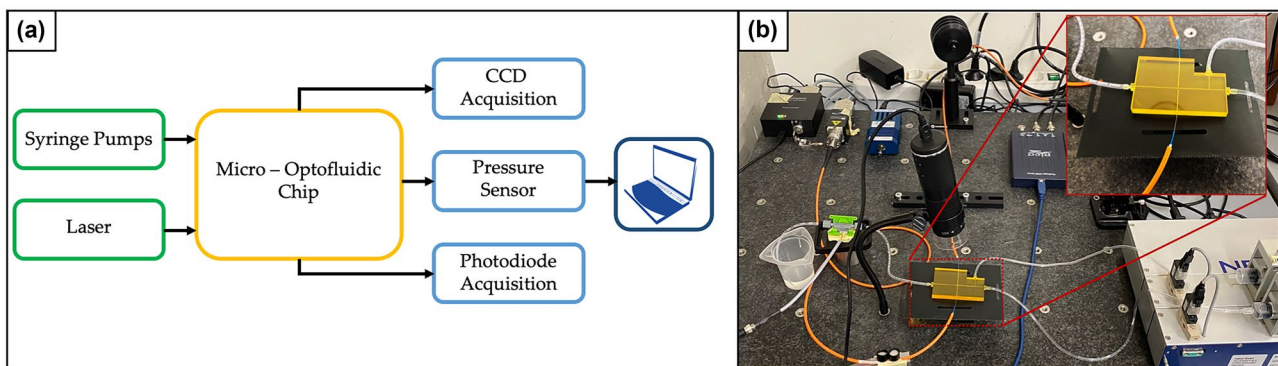
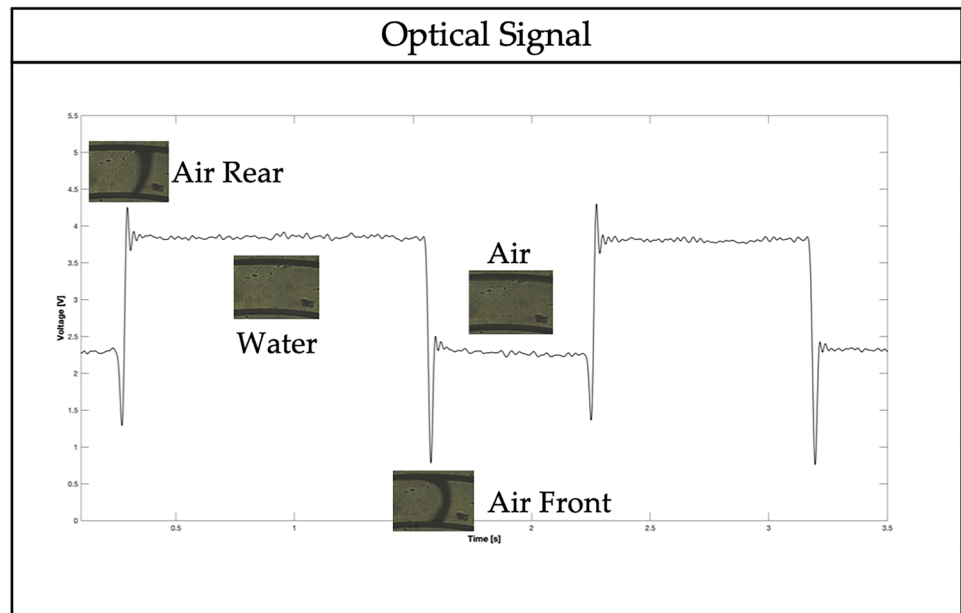


Fig. 5 Experimental setup: (a) block scheme and (b) real picture

**Fig. 6** Optical acquired signal interpretation by acquired CCD video frames



Russia) to characterize surface's roughness [41] and static water angle to measure hydrophilicity.

The AFM test was run in semi-contact mode, with a rate equal to 0.5 Hz, and by using a tip ETALON series (NT-MDT, Zelenograd, Russia) characterized by a resonant frequency of  $140 \pm 10\%$  kHz. The software used to measure the surface roughness in AFM figure is Image Analysis of Nova Px. In the AFM analysis, a  $5 \times 5 \mu\text{m}^2$  area was investigated. For each analysis, three parameters were evaluated, which are the roughness distribution in the square surface (RMS), average roughness (RA), and the peak to peak parameter. All the characterized surfaces were obtained from the processing methods reported above without any further treatment.

Static water contact angle ( $\theta$ ) measurements were run to evaluate the surface hydrophilicity of the two used materials. A Lite Optical Tensiometer TL100 with an accuracy of  $\pm 3^\circ$ , at room temperature and in air atmosphere, was used for the experiments. The test was carried out as follows: first, 5  $\mu\text{L}$  of Milli-Q water drop, having a resistivity equal to 18.2  $\text{M } \Omega$  at 25  $^\circ\text{C}$ , was deposited on the device's surface with a calibrated micro-syringe; next, measurements of  $\theta$  were made on both sides of the two-dimensional projection of the droplet. Five different sets of measurements have been performed on different surface portions of every sample to obtain statistically reliable results.

### 3.4 PDMS and HTL resin transparency evaluation

In order to assess the optical properties of the two investigated materials for the realization of the micro-optofluidics devices, a transmission analysis was carried out using a spectrometer (USB2000, Ocean Optics, Dunedin, Florida).

The Ocean Optics Transmission Probe (T200-RT-VIS-NIR, Ocean Optics, Dunedin, Florida) is connected to a halogen light source (LS-1, Ocean Optics, Dunedin, Florida) and to the spectrometer. The probe has two fibers with a diameter of about 200  $\mu\text{m}$ : one illuminates the sample and the other one allows the operation of reading. The transmission is the percentage of energy passing through a system relative to the amount that passes through a reference. In the analysis, the reference sample of Polytetrafluoroethylene (PTFE) was considered in order to calibrate the instrument at a transmission value of 100%. After the operation of calibration, the measurements were taken from the two materials.

## 4 Results and discussion

### 4.1 Surface analysis

For many applications in microfluidic technology, the behavior at the solid–liquid interface is of relevant importance. For example, changes in the fluid wetting ability may affect the exchange momentum of the fluid with the solid surface at the atomic scale, resulting in a velocity slip at the solid wall. Thus, considering that in this paper water is the main flowing fluid, it is important to measure the solid surface behavior. To be more specific, hydrophilic surfaces are more attractive toward water since, being they bear electric charges or polar groups, water molecules interact favorably with them. Instead, hydrophobic surfaces are water unattractive because, being them non polar, they cause water molecules to lack of hydrogen bonding partners [42, 43].

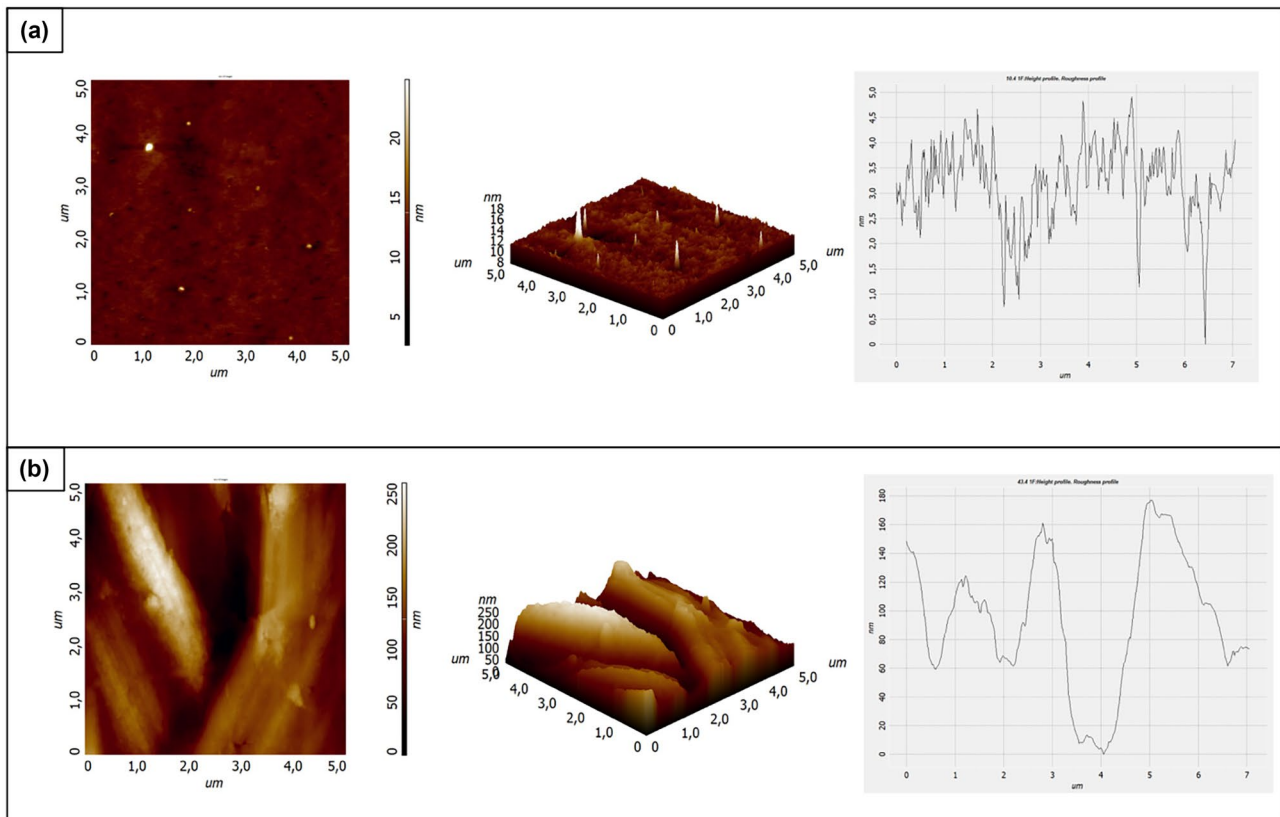


**Fig. 7** Roughness measurements of (a) PDMS and (b) HTL resin surface

Moreover, the flow characteristics in micro-channels may be different from the classical theory for macro-channels. Many experimental and numerical results demonstrated that the friction factor is much higher in micro-channels than in macro-ones [44]. In this context, the surface roughness is of fundamental importance for the understanding of these deviations, since by reducing the channel dimensions, the roughness importance increases. For all these reasons, both the static water contact angle and surface roughness must be evaluated to gain a complete understanding of the hydrodynamic nature of the two-phase fluid into the micro-channels of the two studied devices.

The surface roughness of the PDMS and HTL resin was evaluated using Atomic Force Microscopy (AFM). In AFM, the probe tip is fixed to a cantilever beam. The probe interacts with the surface and the resulting force deflects the beam in a repulsive manner, as described by Hooke's Law. In the same manner that a spring changes dimensions under the influence of forces, the attractive and repulsive forces between atoms of the probe and the surface can also be monitored when brought extremely close to each other. Hence, the net forces acting on the probe tip deflect the cantilever, and the tip displacement is proportional to the force between the surface and the tip. As the probe tip is scanned

across the surface, a laser beam reflects off the cantilever. By monitoring the net ( $x$ ,  $y$ , and  $z$ ) deflection of the cantilever, a three-dimensional image of the surface is constructed [45].

The obtained results from AFM analysis are shown in Fig. 7a for the PDMS and in Fig. 7b for the HTL resin.

The surface roughness of the HTL resin is higher than the PDMS ones (Table 1), in fact both the RMS and the RA parameters evaluated for the HTL resin are the 97% higher than the PDMS ones. Moreover, according to the results, while for the HTL resin a thick web of filaments was spotted on the surface, the PDMS one appeared strongly flatter. While for PDMS, the analysis revealed the presence of some scattered nanometric bubbles which can originate from entrapped air or residual solvent. The PDMS surface roughness analyzed with the AFM is the surface in contact with the 3D-printed mold. In literature, the PDMS surface roughness values obtained for many 3D-printed microfluidic devices are

**Table 1** AFM analysis results for PDMS and HTL photocurable resin

| Material investigated | RMS [nm] | RA [nm] | Peak to peak [nm] |
|-----------------------|----------|---------|-------------------|
| PDMS                  | 1.097    | 0.763   | 35.158            |
| HTL resin             | 47.056   | 37.324  | 259.121           |



**Table 2** Contact angle measurement results for PDMS and HTL photocurable resin

| Material Investigated | CA [°] |
|-----------------------|--------|
| PDMS                  | 111.84 |
| HTL Resin             | 64.36  |

of the order of about  $\sim 2 \mu\text{m}$  [46, 47]. An UV gel smoothing technique allowed to change the surface roughness from 70 to 3 nm [48]. In this work, an UV treatment was applied to the 3D master achieving a PDMS surface roughness of 1 nm.

The relative roughness of the microfluidic channels can be measured as the ratio between the RA parameter and the side of the channel (this being a square section). This parameter can be used to evaluate the flow stability in the microchannel. For the studied surfaces, the relative roughness was equal to 0.0001% and 0.0002% for PDMS and HTL resin, respectively. In other papers, relative roughness values of the order of magnitude of the micrometer were reported showing, for the devices, an increase of 8–38% for the friction factors over the classical theory [49, 50]. Therefore, the values measured here let to conclude that there will be no instability of the flow inside the channel, i.e. flow slowdown or inhibition, for the manufactured devices. These measurements showed that both the used manufacturing techniques can guarantee a stable flow inside the microchannel.

The water angle contact measurements are shown in Table 2. The contact angle for the PDMS was equal to  $111.84^\circ$ , while the HTL resin presented a value of  $64.36^\circ$ .

The micro-optofluidic devices have been tested by using an aqueous two-phase system. In some previous studies, high water angle contacts showed advantageous results because when the aqueous droplets encounter a wall, they bounce off instead of sticking [51]. In other studies, low water contact angles resulted in some flow complications due to the adhesion of water droplets to the wall [52, 53]. In order to unveil issues with flow advancement and process stability within the channel, slug flow detection set up for *Device 2* was studied as reported in the following.

## 4.2 Optimization of the slug flow detection set up for the Device 2

To optimize the slug flow detection set up for the *Device 2*, a replicated general factorial design was carried out. Two design factors (independent variables) have been considered for the test procedure: the laser input power (factor A) and the fluid flow rate (factor B). While factor A has been varied at two levels ( $a = 2$ ), factor B has been varied at three levels ( $b = 3$ ). The  $a = 2$  levels correspond to 1 mW and 5 mW, respectively. The  $b = 3$  levels correspond to {0.1, 0.2, 0.3} ml/min. The number of replications has been set equal to  $n = 3$ , for a total of  $N = a \times b \times n = 18$  experimental runs. The experimental plan is summarized in Table 3.

Next, the following responses (dependent variables) have been considered for the experimental plan:

- The voltage difference ( $\Delta V$ ) is defined as the difference between the grand averages of the observations measured at the high and the low level of the square wave optical signal, respectively. The calculation of the voltage difference ( $\Delta V$ ) is as follows: by starting from the optical signal acquisition for a period of 15 s, the signal is post-processed as previously described. Next, in each acquired and post-processed optical signal, the sequence of high-level values in the wave square is collected in a time order, thus getting a single sample of  $V_h(i)$  observations, for  $i = 1, \dots, N_h$ . The same procedure is performed for the low levels of the square wave, thus obtaining a single sample of  $V_l(i)$  observations, for  $i = 1, \dots, N_l$ . Here  $N_h \in (2, 5 \cdot 10^3, 10^4)$  and  $N_l \in (2, 5 \cdot 10^3, 10^4)$ . Next, the corresponding sample mean values ( $\bar{X}_h$  and  $\bar{X}_l$ ) and sample standard deviations ( $s_h$  and  $s_l$ ) are evaluated for each

**Table 3** Experimental plan: factors and levels

| Factor            | Symbol | Type      | Unit     | Low level (-1) | Center level (0) | High level (+1) |
|-------------------|--------|-----------|----------|----------------|------------------|-----------------|
| Laser input power | A      | Numerical | [mW]     | 1              | -                | 5               |
| Flow rate         | B      | Numerical | [ml/min] | 0.1            | 0.2              | 0.3             |

sample  $V_h(i)$  and  $V_l(i)$ , respectively. Having both  $V_h(i)$  and  $V_l(i)$  a very large number of observations, both their sample means ( $\bar{V}_h$  and  $\bar{V}_l$ ) are approximately normal random variables with estimated parameters:

$$\begin{cases} \bar{V}_h \sim N\left(\bar{X}_h, \frac{s_h^2}{N_h}\right) \\ \bar{V}_l \sim N\left(\bar{X}_l, \frac{s_l^2}{N_l}\right) \end{cases}$$

Starting from this assumption, the response  $\Delta V$  is a normal random variable having distribution:

$$\Delta V = \bar{V}_h - \bar{V}_l \sim N\left(\bar{X}_h - \bar{X}_l, \frac{s_h^2}{N_h} + \frac{s_l^2}{N_l}\right)$$

- The second investigated response is the mean period ( $T_{ph}$ ) associated to a complete air–water slug passage, obtained as the reciprocal of the frequency peak gained from the amplitude spectrum of the acquired optical signal:

$$T_{ph} = \frac{1}{f_{ph}} = \langle T_w \rangle + \langle T_a \rangle$$

In particular, the first response  $\Delta V$  is considered to show that the optical part of the device is really able to discriminate between the two fluids that make up the slug flow. While the second response  $T_{ph}$  is taken into account to evaluate if a real hydrodynamic stability is achieved into the micro-channel.

Once the response observations have been calculated, an Analysis of Variance (ANOVA) study has been performed to investigate the statistical significance of each factor and their interaction. The observations regarding the first response,

**Table 4** Observations  $\Delta V$  [V] for the investigated scenarios. Factors: Input Power (P) and Flow Rate (FR).  $P = \{1, 5\}$  mW;  $FR = \{0.1, 0.2, 0.3\}$  ml/min

|                  |   | Flow Rate [ml/min] |                    |                    |
|------------------|---|--------------------|--------------------|--------------------|
|                  |   | 0.1                | 0.2                | 0.3                |
| Input Power [mW] | 1 | (1.59, 1.75, 1.47) | (1.47, 1.69, 1.25) | (1.37, 1.52, 1.42) |
|                  | 5 | (2.92, 2.73, 3.51) | (2.69, 2.72, 3.05) | (2.54, 2.51, 3.39) |

for all the investigated scenarios and all the run replications, are summarized in Table 4. While the ANOVA table for the  $\Delta V$  response and a bar plot comparing the various cases are shown in Table 5 and Fig. 8, respectively.

From the ANOVA study shown in Table 5, the laser input power (factor A) is the only influential factor ( $p$ -value  $< 0.001$ ) on voltage difference. Both the R-squared and the adjusted R-squared have high values ( $R^2 = 0.89$ ,  $R^2_{adj} = 0.87$ ); thus, most of the variability in the observations is explained by the laser input power. From the model adequacy checking on the residuals, no anomalies were identified. Deeper investigation on the obtained results shows that by increasing the input power of the laser, the gap existing between the averages at the high and low levels of the square wave optical signal almost doubles. This results in a higher discrimination power of *Device 2* between air and water. However, increasing the input power leads to a slightly higher dispersion in the observations. When the laser power is at the low level, the discrimination power is still sufficient. Therefore, it is convenient to design a higher laser input power for all those scenarios where the difference between the refractive indexes of the two investigated fluids is narrow.

The observations obtained for the mean period ( $T_{ph}$ ) are summarized in Table 6 and shown in Fig. 9. The results of the ANOVA study are shown in Table 7.

The flow rate (factor B) is the only statistically influencing factor on the mean period, as shown in the ANOVA

**Table 5** ANOVA table for the response voltage difference ( $\Delta V$ )

| Source               | Sum of squares | df | Mean square | F value  | p-value    |
|----------------------|----------------|----|-------------|----------|------------|
| Model                | 8.854417       | 2  | 4.427208    | 60.70683 | $< 0.0001$ |
| A-input power        | 8.72826        | 1  | 8.72826     | 119.6838 | $< 0.0001$ |
| B-flow rate          | 0.126157       | 1  | 0.126157    | 1.729892 | 0.2082     |
| Residual             | 1.093915       | 15 | 0.072928    |          |            |
| Lack of fit          | 0.035664       | 3  | 0.011888    | 0.134802 | 0.9374     |
| Pure error           | 1.058252       | 12 | 0.088188    |          |            |
| Cor total            | 9.948332       | 17 |             |          |            |
| <b>R-squared</b>     | 0.8900         |    |             |          |            |
| <b>Adj R-squared</b> | 0.8754         |    |             |          |            |

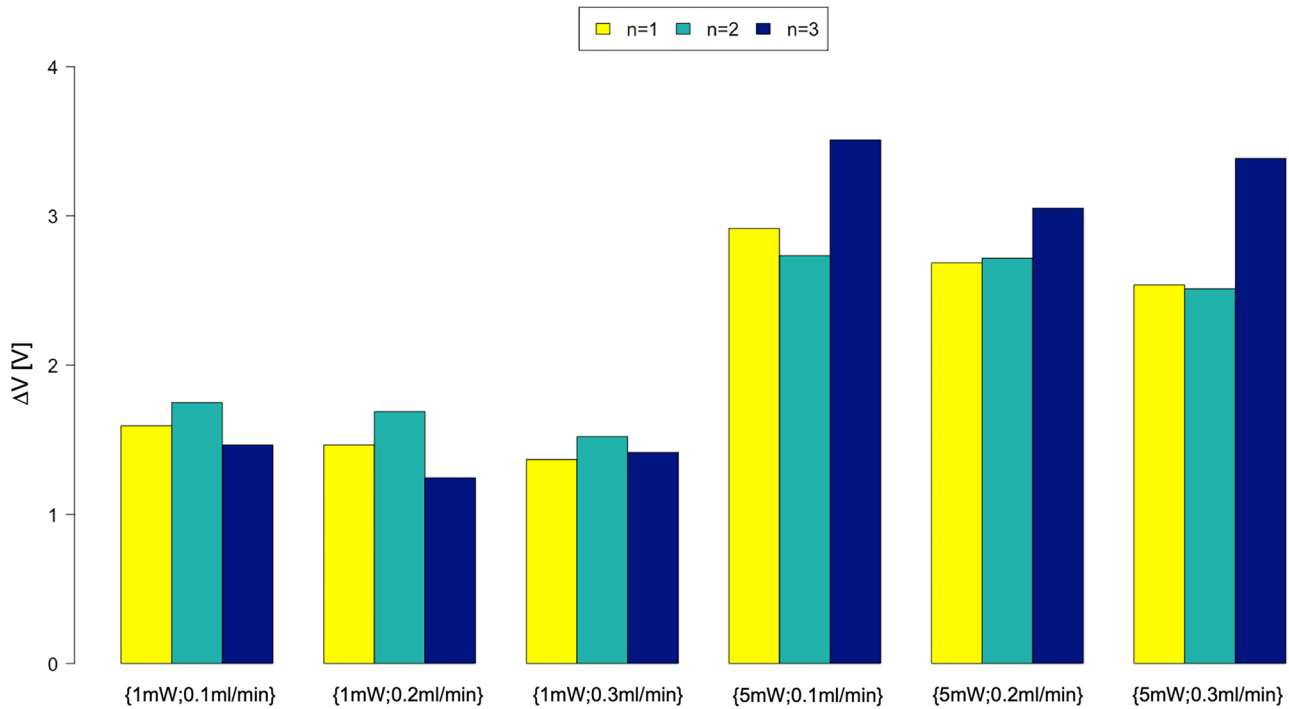


**Fig. 8** Bar plot showing the voltage difference ( $\Delta V$ ), for each investigated scenario and replication. Bar errors have not been added because they were strongly narrower than the bar height

study (Table 7). Although the parameter laser input power (factor A) is clearly not influential ( $p$ -value  $> 0.001$ ) on the mean period, it has been considered in the study to account for the possibility that at higher power values, the fluid would be heated more, with a consequent lower viscosity value and a higher fluid velocity. No anomalies have been found from the model adequacy checking on the residuals. Both the R-squared and the adjusted R-squared have quite high values ( $R^2 = 0.75$ ,  $R^2_{adj} = 0.71$ ). The flow stability is significantly improved at higher values of the flow rate, thus suggesting designing a flow rate equal to 0.3 ml/min.

Summarizing the results obtained from the two responses, it is reasonably legitimate to assume that a good test configuration for the micro-optofluidic device should consider  $(P, FR) = (5 \text{ mW}, 0.3 \text{ ml/min})$ .

The optical signals and the corresponding amplitude spectrums related to the optimal operative condition are shown in Fig. 10. The same plots for the other operative conditions are available in the [supplementary material](#). Looking at them, it is possible to discriminate each fluid of the two-phase flow. Even though the discrimination between air and water is always possible, the maximum and minimum levels of the square wave optical signals are not always at the same level by repeating the signal acquisition under the same conditions. This phenomenon can be attributed to centering problems between

the two optical fibers (input and output) since, once inserted in the appropriate device’s slots, a little mechanical backlash occurs. Nevertheless, what matters most is that, by focusing on the first investigated response (i.e., voltage difference  $\Delta V$ ), a reasonable repeatability at the same process condition for all the replications run was spotted.

### 4.3 Comparative analysis between Device 1 and Device 2

Once the optimal operative condition was identified for the *Device 2*, a comparison was carried out with *Device 1*. The aim is to identify the most performing device and the one affected by the lower repeatability error. The comparison

**Table 6**  $T_{ph}$  observations for the investigated scenarios. Factors: Input Power (P) and Flow Rate (FR).  $P = \{1, 5\}$  mW;  $FR = \{0.1, 0.2, 0.3\}$  ml/min

|                  |   | Flow Rate [ml/min] |                    |                    |
|------------------|---|--------------------|--------------------|--------------------|
|                  |   | 0.1                | 0.2                | 0.3                |
| Input Power [mW] | 1 | (1.88, 1.87, 1.14) | (0.60, 0.94, 0.60) | (0.37, 0.50, 0.47) |
|                  | 5 | (1.87, 1.87, 1.13) | (0.63, 0.91, 0.60) | (0.37, 0.65, 0.47) |

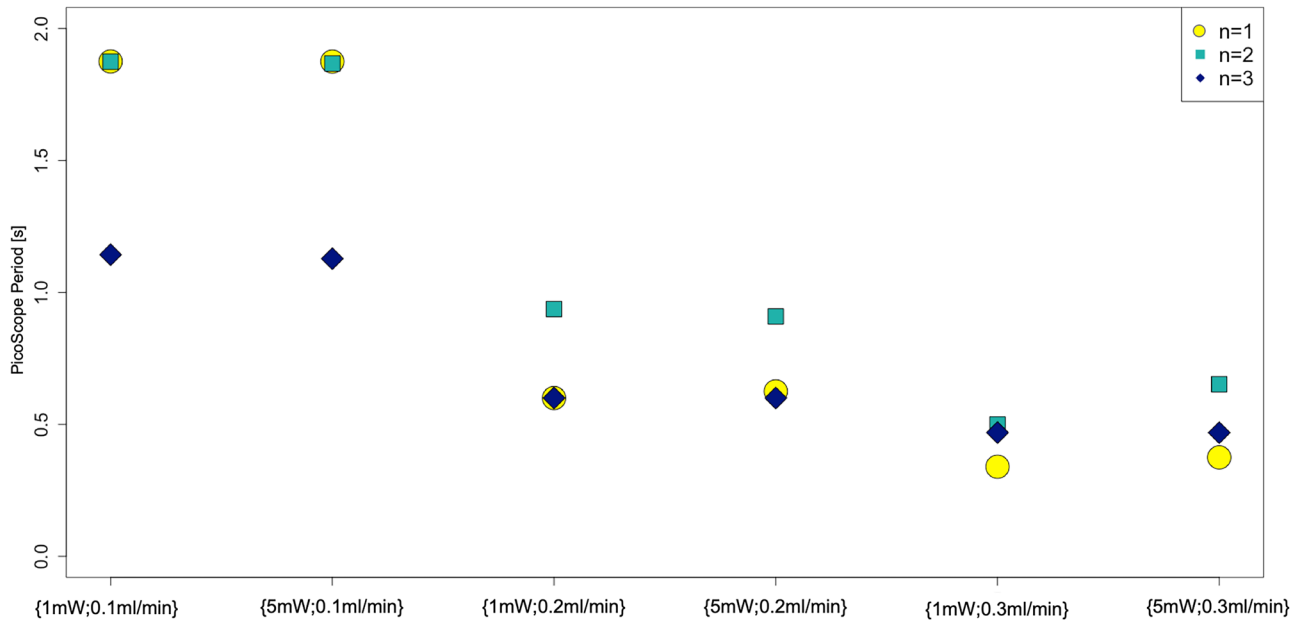


**Fig. 9** Trend related to the mean period ( $T_{ph}$ ) associated to a complete air–water slug passage for each investigated scenario and replication.  $n = 1, 2, 3$  refer to the three run replications

between the two devices was carried out for all the investigated responses. The chosen test set up for the comparison was  $(P, FR) = (5 \text{ mW}, 0.3 \text{ ml/min})$ . This decision is justified by the fact that setting the flow rate equal to  $0.3 \text{ ml/min}$  showed to be the best operative condition for improving the flow stability while choosing the laser power equal to  $5 \text{ mW}$  allowed to have the highest discrimination between air and water levels.

The results relating to the voltage difference ( $\Delta V$ ) are summarized in Table 8 and in Fig. 11. The  $\Delta V$  parameter is always higher for the *Device 1*, having an average value equal to  $7.94 \text{ V}$ , compared to the *Device 2*, which has a mean value equal to  $2.81 \text{ V}$ . This result means that *Device*

*1* better discriminates the two investigated fluids, since the gap between the high and the low level of the square wave optical signal is larger. This result is justifiable by the fact that the PDMS is fully transparent, while the HTL resin is not, as shown in Fig. 12. In order to assess the optical properties of the two investigated materials, a transmission analysis was carried out using a spectrometer (USB2000, Ocean Optics, Dunedin, Florida). Considering a reference sample with 100% of transmission, a value of 126% was obtained for the PDMS and 17% for the HTL resin. This result states a difference of transparency between the two materials and it can be also seen in Fig. 12 where the fibers' insertions and the channel are clearly visible in the PDMS device in contrast to the HTL resin device. However, the dispersion of observations collected by using the *Device 2* ( $\sigma = 0.50$ ) is much smaller than *Device 1* ( $\sigma = 1.72$ ). This result can be explained by considering that while the *Device 2* is manufactured with a high stiffness resin having a Young's Modulus value equal to  $1.32 \text{ MPa}$ , the *Device 1* is made of a flexible material which is characterized by a Young's Modulus of  $3.9 \text{ MPa}$ . Thus, the use of the PDMS device can lead to difficulties in centering the two optical fibers with a greater probability, because as soon as the optical fibers are inserted into the micro-channels (having a length ranging between  $16$  and  $23 \text{ mm}$ ), they tend to flex the device in an easier way for PDMS material than HTL resin. For this reason, the alignment can lead to difficulties in centering the two optical fibers resulting in higher variations for the measurements obtained.

**Table 7** ANOVA table for the response mean period ( $T_{ph}$ )

| Source               | Sum of squares | df | Mean square | F value  | p-value |
|----------------------|----------------|----|-------------|----------|---------|
| Model                | 4.001519       | 2  | 2.00076     | 21.92583 | <0.0001 |
| A-input power        | 0.000931       | 1  | 0.000931    | 0.010199 | 0.9209  |
| B-flow rate          | 4.000589       | 1  | 4.000589    | 43.84147 | <0.0001 |
| Residual             | 1.368769       | 15 | 0.091251    |          |         |
| Lack of fit          | 0.458317       | 3  | 0.152772    | 2.013578 | 0.1658  |
| Pure error           | 0.910452       | 12 | 0.075871    |          |         |
| Cor total            | 5.370288       | 17 |             |          |         |
| <b>R-squared</b>     | 0.7451         |    |             |          |         |
| <b>Adj R-squared</b> | 0.7111         |    |             |          |         |

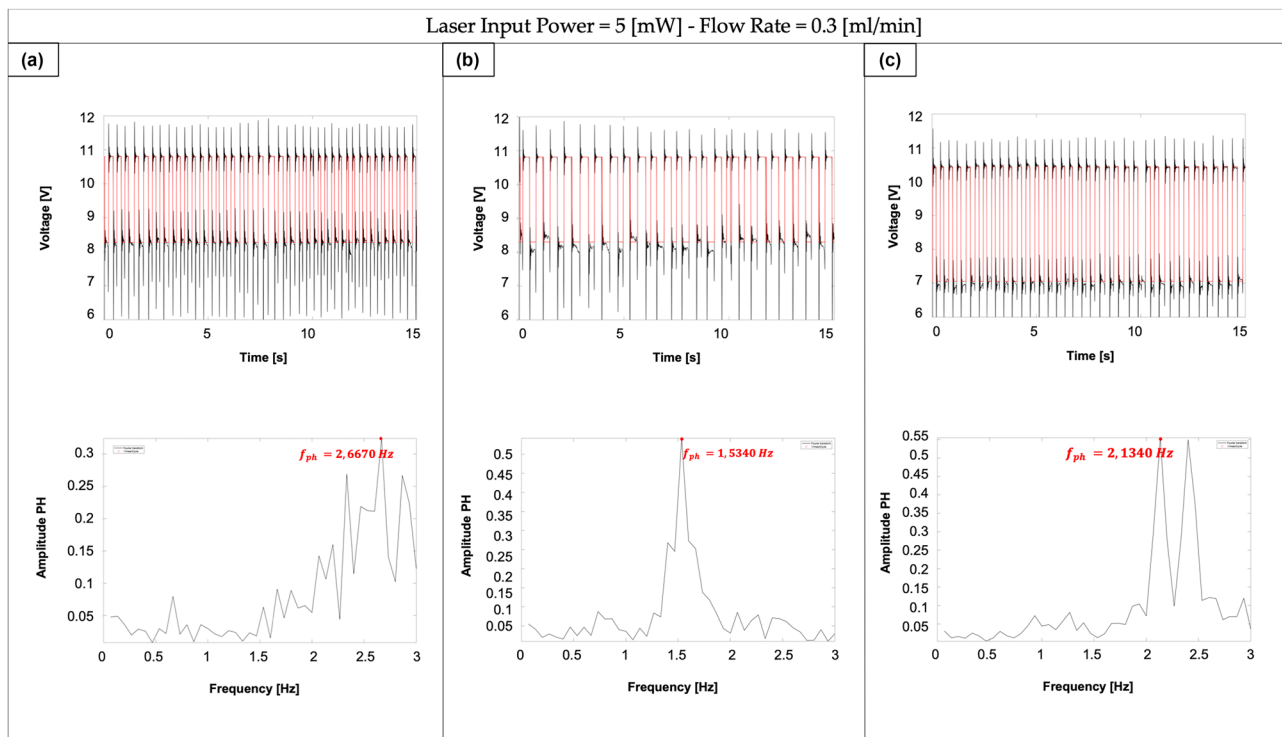


**Fig. 10** Optical signals in the time domain (upper row) with (P, FR)=(5 mW, 0.3 ml/min) and optical signals (lower row) in the frequency domain with (P, FR)=(5 mW, 0.3 ml/min) for each rep-

lication: **a**  $n=1$ , **b**  $n=2$ , and **c**  $n=3$ . The three identified peaks are necessary to evaluate the mean period ( $T_{ph}$ ) associated to a complete air–water slug passage

Once again, consistent with what has been said so far, the same reasoning can be made for the second investigated response, i.e., the mean period  $T_{ph}$ . In fact, according with the results summarized in Table 9 and shown in Fig. 13, the observed data for the *Device 1* present a higher dispersion than *Device 2*. Thus, *Device 2* shows a greater flow stability than *Device 1*. Even though the PDMS surface properties related to the angle of contact measurements should have allowed for a faster slug flow than the HTL resin device, being the PDMS surface hydrophobic and the HTL resin one hydrophilic, an opposite trend was shown by the experimental results obtained for the mean period  $T_{ph}$ . Indeed, the

mean period value for the *Device 2* is approximately equal to 12% the value for *Device 1*.

**Table 8** A comparison between the *Device 1* and the *Device 2* regarding the voltage difference ( $\Delta V$ )

|                 |                    |                  | $n=1$          | $n=2$          | $n=3$          |
|-----------------|--------------------|------------------|----------------|----------------|----------------|
| ID [-]          | Flow Rate [ml/min] | Input Power [mW] | $\Delta V$ [V] | $\Delta V$ [V] | $\Delta V$ [V] |
| <i>Device 1</i> | 0.3                | 5                | 7.80           | 6.29           | 9.73           |
| <i>Device 2</i> | 0.3                | 5                | 2.54           | 2.51           | 3.39           |

Although the results relating to this last comparison may appear contradictory with what has been said previously regarding the chemical nature of the identified surfaces, since the flow is slower in the *Device 1* than in *Device 2*, a further important aspect must be considered. The design of the macro-to-micro interface, that is the inlets connecting the micro-optofluidic device to the fluid-loading tubes, implemented in the two analyzed devices is different. In fact, while the vertical (top-loading) inlet approach was used for the *Device 1*, the parallel (in-line) ones were used for the *Device 2*. According with a previous study run for similar flow velocity range [54], the design decision for the *Device 2* made it possible to obtain a maximum speed in the center of the channel and along itself. Instead, the approach used for the inlets in *Device 1* was able to obtain a maximum flow speed only in correspondence of the macro-to-micro interface, which adequately justifies the obtained results.

In conclusion, a comparison between the main properties for each of the two analyzed devices is summarized in Table 10.



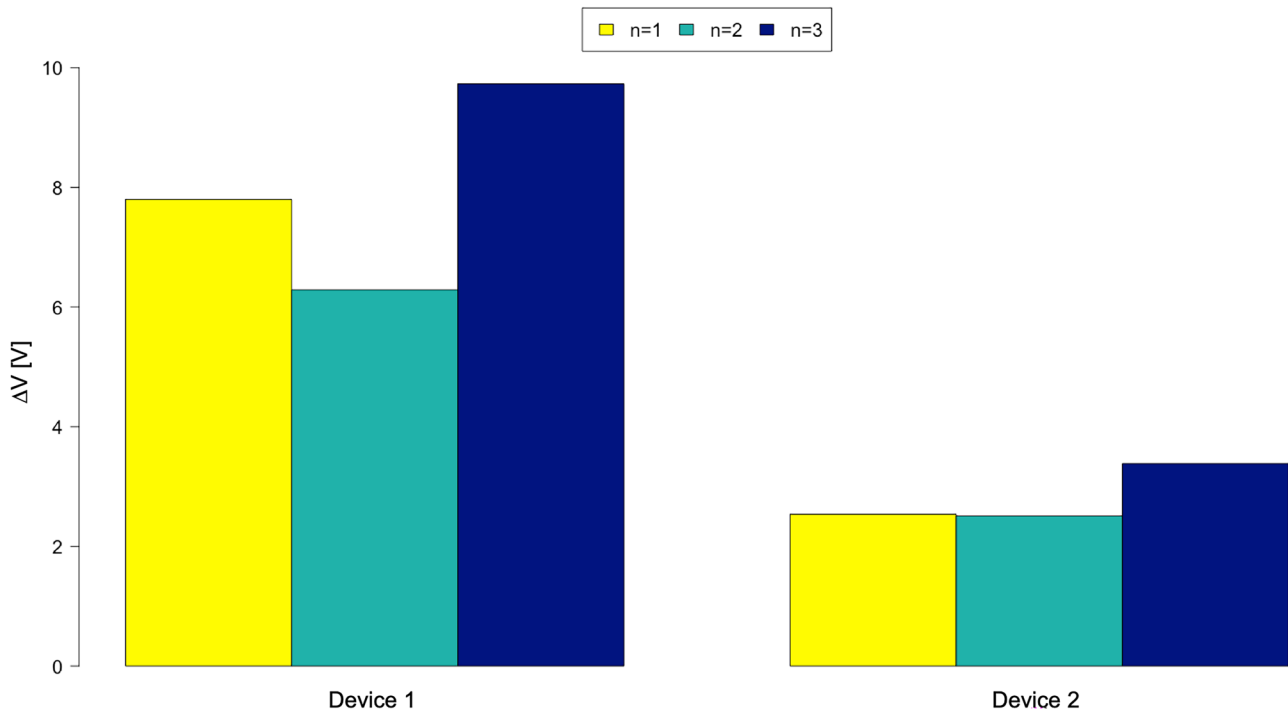


**Fig. 11** Bar plot comparing the *Device 1* (PDMS) and the *Device 2* (HTL resin) with respect to the first investigated response, i.e., the Voltage Difference ( $\Delta V$ ), for each replication. Bar errors have not been added because they were strongly narrower than the bar height

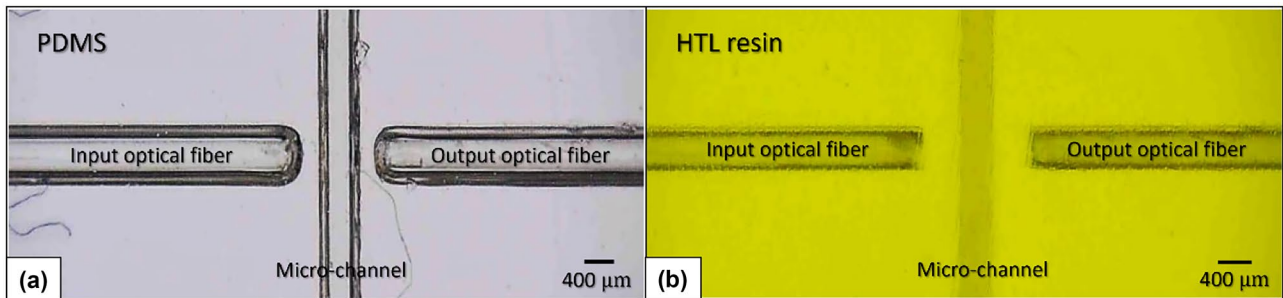


**Fig. 12** The images of the *Device 1* (PDMS) (a) and the *Device 2* (HTL resin) (b) showing the area which includes the micro-channel and the optical fibers inserted and aligned, dedicated for the monitoring of the slug flow process

**Table 9** A comparison between the *Device 1* (PDMS) and the *Device 2* (HTL resin) regarding the mean period associated to a complete air–water slug passage ( $T_{ph}$ )

| ID [-]          | Flow rate [ml/min] | Input power [mW] | n = 1        | n = 2        | n = 3        | Mean [s] |
|-----------------|--------------------|------------------|--------------|--------------|--------------|----------|
|                 |                    |                  | $T_{ph}$ [s] | $T_{ph}$ [s] | $T_{ph}$ [s] |          |
| <i>Device 1</i> | 0.3                | 5                | 4.95         | 4.29         | 3.03         | 4.09     |
| <i>Device 2</i> | 0.3                | 5                | 0.37         | 0.65         | 0.47         | 0.50     |

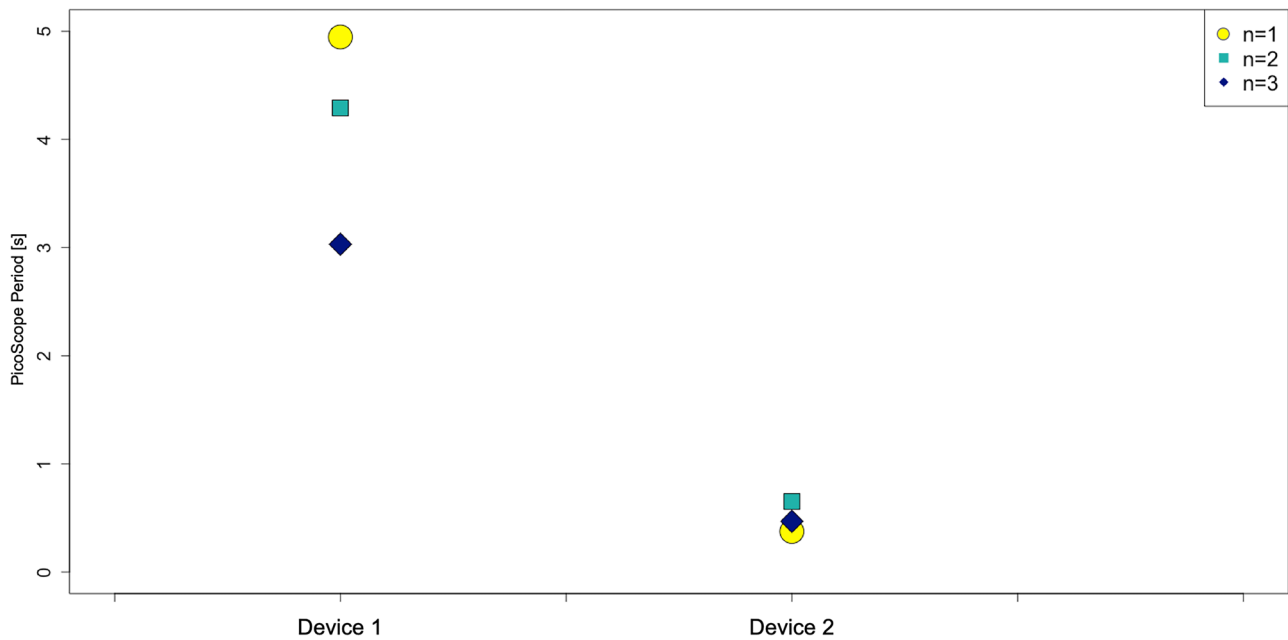


**Fig. 13** Comparison of the trend related to the mean period ( $T_{ph}$ ) associated to a complete air–water slug passage between the *Device 1* (PDMS) and the *Device 2* (HTL resin)

**Table 10** A comparison between the *Device 1* and the *Device 2* in terms of main properties

| Technologies           | Fabrication process   | Steps of the manufacturing process | Contact angle [°] | Relative roughness [%] | Young's Modulus [MPa] | Elongation at break [%] | Transparency [%] |
|------------------------|-----------------------|------------------------------------|-------------------|------------------------|-----------------------|-------------------------|------------------|
| PDMS-based 3D printing | Master–slave approach | 6                                  | 111.84            | 0.0001                 | 1.32                  | 100                     | 126              |
| HTL resin 3D printing  | Direct printing       | 2                                  | 65.36             | 0.0002                 | 3.90                  | 3                       | 17               |

## 5 Conclusions

In this work, two micro-optofluidic flow devices were manufactured and fully characterized. A novel approach based on the Projection Micro Stereolithography (P $\mu$ SL) 3D printing approach was compared to a novel master–slave 3D printing approach developed by the authors [39]. The P $\mu$ SL 3D printing approach allowed to obtain in one-step the final device skipping all in once the manual steps which are required by the other considered procedure. In addition to that, the possibility to design and print complex geometries allowed to fully integrate coaxial inlets and outlets thus overcoming a design limitation of the master–slave approach.

The materials used for the two approaches differed in terms of roughness and water contact angle. In particular, the relative roughness for the two materials ranged between 0.0001 and 0.0002% for PDMS and HTL resin, respectively. These values mean that no flow instability inside the micro-channel would be associated to the solid surface making

both the materials suitable, in terms of their surface finishing, for microfluidic devices.

The device obtained via P $\mu$ SL was tested for the slug flow detection using the same set up used previously for the PDMS-based devices [39]. The operative conditions used for the flow detection were optimized using ANOVA to rationalize the effect of each varied parameter on the selected responses. The input laser power and the flow rate levels of 5 mW and 0.3 ml/min were found as the best operative conditions to improve the discrimination between both fluids and the flow stability.

The performance of the two devices as slug flow detector was analyzed using the optimized operative conditions. The comparison revealed that the *Device 2*, being fabricated with a stiff resin embedding the coaxial inlets and outlets, returned lower dispersed data compared to *Device 1*. While, *Device 1* presented higher  $\Delta V$  values resulting in a better discrimination of the two investigated fluids due to its higher value for transparency. The findings of the comparative

analysis allowed to highlight the advantages and disadvantages of the two approaches proposed. The advantages of P $\mu$ SL are its suitability to print with high accuracy and in one step complex micro-optofluidic devices. However, the use of HTL resin with lower transparency compared to PDMS results in a lower detection performance requiring the use of higher input laser power. Therefore, future research activity must be driven toward the development of resin's grades for 3D printing showing the same optical properties of PDMS. Moreover, further studies should take into account the multi-material strategy, in order to create plastic optical fibers (POFs) totally integrated into the 3D-printed micro-optofluidic device as a possible solution to alignment problems presented in this work. Similar studies have already been carried out by the authors [55], where a 3D-printed sensor was obtained by exploiting the inkjet technique. In conclusion, customized surface's chemical functionalization can be further developed in order to improve the slug flow control, for example, by accelerating or slowing down the flow by making use of suitable wall–fluid chemical interactions.

**Supplementary Information** The online version contains supplementary material available at <https://doi.org/10.1007/s00170-022-08889-8>.

**Author contribution** Lorena Saitta, paper writing and experimental testing; Matteo Barcellona conducted the AFM testing; Giovanna Stella conducted the microfluidic testing; Maide Bucolo reviewed the paper; Giovanni Celano carried out statistical analysis; Gianluca Cicala, paper review; Maria Elena Fragalà, project management; and Claudio Tosto performed device design.

**Funding** Open access funding provided by Università degli Studi di Catania within the CRUI-CARE Agreement. The authors acknowledge the funding received on this project from Università degli Studi di Catania under the Grant Scheme PIACERI with the project MAF-moF “Materiali multifunzionali per dispositivi micro-optofluidici” Project Coordinator Maria Elena Fragalà. Gianluca Cicala also acknowledges Italian MIUR grant number 20179SWLKA Project Title Multiple Advanced Materials Manufactured by Additive technologies (MAMMA), under the PRIN funding Scheme. Gianluca Cicala acknowledges Boston Micro Fabrication (Maynard, Massachusetts) for the 3D-printed micro-optofluidic device provided to perform the experimental tests.

**Availability of data and materials** Data are fully available and can be shared openly.

**Code availability** Code is custom-made and it cannot be shared as it is a proprietary.

## Declarations

**Ethics approval** The paper does not request for ethics approval.

**Consent to participate** No.

**Consent for publication** Yes.

**Conflict of interest** The authors declare no competing interests.

**Open Access** This article is licensed under a Creative Commons Attribution 4.0 International License, which permits use, sharing, adaptation, distribution and reproduction in any medium or format, as long as you give appropriate credit to the original author(s) and the source, provide a link to the Creative Commons licence, and indicate if changes were made. The images or other third party material in this article are included in the article's Creative Commons licence, unless indicated otherwise in a credit line to the material. If material is not included in the article's Creative Commons licence and your intended use is not permitted by statutory regulation or exceeds the permitted use, you will need to obtain permission directly from the copyright holder. To view a copy of this licence, visit <http://creativecommons.org/licenses/by/4.0/>.

## References

1. Scott SM, Ali Z (2021) Fabrication methods for microfluidic devices: an overview. *Micromachines* 12. <https://doi.org/10.3390/mi12030319>
2. Zhou W, Le J, Chen Y et al (2019) Recent advances in microfluidic devices for bacteria and fungus research. *TrAC Trends Anal Chem* 112:175–195. *TrAC Trends Anal Chem* 112:175–195. <https://doi.org/10.1016/J.TRAC.2018.12.024>
3. McDonald JC, Duffy DC, Anderson JR, Chiu DT, Wu H, Schueller OJWG (2000) Fabrication of microfluidic systems in poly(dimethylsiloxane) - PubMed. *Electrophoresis* 21:27–40. [https://doi.org/10.1002/\(SICI\)1522-2683\(20000101\)21:1%3c27::AID-ELPS27%3e3.0.CO;2-C](https://doi.org/10.1002/(SICI)1522-2683(20000101)21:1%3c27::AID-ELPS27%3e3.0.CO;2-C)
4. Fiorini GS, Chiu DT (2005) Disposable microfluidic devices: fabrication, function, and application. *Biotechniques* 38:429–446. <https://doi.org/10.2144/05383RV02>
5. Whitesides GM (2006) The origins and the future of microfluidics. *Nature* 442:368–373. <https://doi.org/10.1038/nature05058>
6. Convery N, Gadegaard N (2019) 30 years of microfluidics. *Micro Nano Eng* 2:76–91. <https://doi.org/10.1016/j.mne.2019.01.003>
7. Gale BK, Jafek AR, Lambert CJ et al (2018) A review of current methods in microfluidic device fabrication and future commercialization prospects. *Inventions* 3. <https://doi.org/10.3390/inventions3030060>
8. Yin L, Du G, Zhang B et al (2020) Efficient drug screening and nephrotoxicity assessment on co-culture microfluidic kidney chip. *Sci Rep* 10:1–11. <https://doi.org/10.1038/s41598-020-63096-3>
9. Mashaghi S, Abbaspourrad A, Weitz DA, van Oijen AM (2016) Droplet microfluidics: a tool for biology, chemistry and nanotechnology. *TrAC - Trends Anal Chem* 82:118–125. <https://doi.org/10.1016/j.trac.2016.05.019>
10. Kristinn B, Minzioni P, Osellame R et al (2017) Roadmap for optofluidics. *J Opt* 19. <https://doi.org/10.1088/2040-8986/2FAA783B>
11. Schembri F, Bucolo M (2011) Periodic input flows tuning nonlinear two-phase dynamics in a snake microchannel. *Microfluid nanofluidics* 11:189–197. <https://doi.org/10.1007/s10404-011-0786-5>
12. Cairone F, Davi S, Stella G et al (2020) 3D-printed micro-optofluidic device for chemical fluids and cells detection. *Biomed Microdevices* 22:1–10. <https://doi.org/10.1007/s10544-020-00487-3>
13. Cairone F, Gagliano S, Carbone DC et al (2016) Micro-optofluidic switch realized by 3D printing technology. *Microfluid nanofluidics* 20:1–10. <https://doi.org/10.1007/s10404-016-1727-0>
14. Harrison DJ, Fluri K, Seiler K et al (1993) Micromachining a miniaturized capillary electrophoresis-based chemical analysis system on a chip. *Science* 261:895–897. <https://doi.org/10.1126/SCIENCE.261.5123.895>

15. Jacobson SC, Hergenroeder R, Koutny LB, Ramsey JM (2002) Open channel electrochromatography on a microchip. *Anal Chem* 66:2369–2373. <https://doi.org/10.1021/AC00086A024>
16. Jacobson SC, Moore AW, Ramsey JM (2002) Fused quartz substrates for microchip electrophoresis. *Anal Chem* 67:2059–2063. <https://doi.org/10.1021/AC00109A026>
17. Matzke CM, Kottenstette RJ, Casalnuovo SA et al (1998) Microfabricated silicon gas chromatographic microchannels: fabrication and performance 3511:262–268. <https://doi.org/10.1117/12.324309>
18. Moore AW, Jacobson SC, Ramsey JM (1995) Microchip separations of neutral species via micellar electrokinetic capillary chromatography. *Anal Chem* 67:4184–4189. <https://doi.org/10.1021/ac00118a023>
19. Tony A, Rasouli A, Farahinia A, et al (2021) Toward a soft microfluidic system: concept and preliminary developments. 27th International Conference on Mechatronics and Machine Vision in Practice (M2VIP):755–759. <https://doi.org/10.1109/M2VIP49856.2021.9665022>
20. Becker H, Gärtner C (2000) Polymer microfabrication methods for microfluidic analytical applications. Wiley Online Library Electrophoresis 21:12–26. [https://doi.org/10.1002/\(SICI\)1522-2683\(20000101\)21:1%3c12::AID-ELPS12%3e3.0.CO;2-7](https://doi.org/10.1002/(SICI)1522-2683(20000101)21:1%3c12::AID-ELPS12%3e3.0.CO;2-7)
21. Chiao Chao T, Ros A (2008) Microfluidic single-cell analysis of intracellular compounds. *J R Soc Interface* 5. <https://doi.org/10.1098/RSIF.2008.0233.FOCUS>
22. Eriksson E, Sott K, Lundqvist F et al (2010) A microfluidic device for reversible environmental changes around single cells using optical tweezers for cell selection and positioning. *Lab Chip* 10:617–625. <https://doi.org/10.1039/B913587A>
23. Zheng B, Roach LS, Ismagilov RF (2003) Screening of protein crystallization conditions on a microfluidic chip using nanoliter-size droplets. *J Am Chem Soc* 125:11170–11171. <https://doi.org/10.1021/JA037166V>
24. Chiu DT, Jeon NL, Huang S et al (2000) Patterned deposition of cells and proteins onto surfaces by using three-dimensional microfluidic systems. *Proc Natl Acad Sci* 97:2408–2413. <https://doi.org/10.1073/PNAS.040562297>
25. Benedetto A, Accetta G, Fujita Y, Charras G (2014) Spatiotemporal control of gene expression using microfluidics. *Lab Chip* 14:1336–1347. <https://doi.org/10.1039/c3lc51281a>
26. Huber DL, Manginell RP, Samara MA et al (2003) Programmed adsorption and release of proteins in a microfluidic device. *Science* 301:352–354. <https://doi.org/10.1126/science.1080759>
27. Stroock AD, Whitesides GM (2003) Controlling flows in microchannels with patterned surface charge and topography. *Acc Chem Res* 36:597–604. <https://doi.org/10.1021/ar0202870>
28. Xia Y, Whitesides GM, (1998) Soft lithography. *Angew Chemie - Int Ed* 37:550–575. [https://doi.org/10.1002/\(sici\)1521-3773\(19980316\)37:5%3c550::aid-anie550%3e3.3.co;2-7](https://doi.org/10.1002/(sici)1521-3773(19980316)37:5%3c550::aid-anie550%3e3.3.co;2-7)
29. Lake M, Lake M, Narciso C et al (2015) Microfluidic device design, fabrication, and testing protocols. *Protoc Exch*. <https://doi.org/10.1038/protex.2015.069>
30. Wolf MP, Salieb-Beugelaar GB, Hunziker P (2018) PDMS with designer functionalities—properties, modifications strategies, and applications. *Prog Polym Sci* 83:97–134. <https://doi.org/10.1016/j.progpolymsci.2018.06.001>
31. Borók A, Laboda K, Bonyár A (2021) PDMS bonding technologies for microfluidic applications: a review. *Biosensors* 11. <https://doi.org/10.3390/bios11080292>
32. Han D, Lee H (2020) Recent advances in multi-material additive manufacturing: methods and applications. *Curr Opin Chem Eng* 28:158–166. <https://doi.org/10.1016/j.coche.2020.03.004>
33. Bhatia SN, Ingber DE (2014) Microfluidic organs-on-chips. *Nat Biotechnol* 32:760–772. <https://doi.org/10.1038/nbt.2989>
34. Yang Q, Lian Q, Xu F (2017) Perspective: fabrication of integrated organ-on-a-chip via bioprinting. *Biomicrofluidics* 11. <https://doi.org/10.1063/1.4982945>
35. Beebe DJ, Mensing GA, Walker GM (2002) Physics and applications of microfluidics in biology. *Annu Rev Biomed Eng* 4:261–286. <https://doi.org/10.1146/annurev.bioeng.4.112601.125916>
36. Alkhalaf Q, Pande S, Palkar RR (2021) Review of polydimethylsiloxane (PDMS) as a material for additive manufacturing. *Lect Notes Mech Eng*:265–275. [https://doi.org/10.1007/978-981-15-6619-6\\_28](https://doi.org/10.1007/978-981-15-6619-6_28)
37. Thakare K, Jerpseth L, Pei Z et al (2021) Bioprinting of organ-on-chip systems: a literature review from a manufacturing perspective. *J Manuf Mater Process* 5. <https://doi.org/10.3390/JMMP5030091>
38. Ho CMB, Ng SH, Li KHH, Yoon YJ (2015) 3D printed microfluidics for biological applications. *Lab Chip* 15:3627–3637. <https://doi.org/10.1039/c5lc00685f>
39. Stella G, Skariya N, Gagliano S, Cicala G, Bucolo M (2021) Micro-optofluidic systems for slug detection. In: MED'21, Puglia (Italy)
40. Shrivastava A (2018) Introduction to plastics engineering. *Introd to Plast Eng*:1–16. <https://doi.org/10.1016/B978-0-323-39500-7.00001--0>
41. Batteries AL, Zhao Y, Sun Y, Wang Y (2018) XPS, SEM, AFM, and nano-indentation characterization for powder recycling within additive manufacturing process XPS, SEM, AFM, and nano-indentation characterization for. <https://doi.org/10.1088/1757-899X/1182/1/012025>
42. Sendner C, Horinek D, Bocquet L, Netz RR (2009) Interfacial water at hydrophobic and hydrophilic surfaces: slip, viscosity, and diffusion. *Langmuir* 25:10768–10781. <https://doi.org/10.1021/LA901314B>
43. Choi C-H, Westin KJA, Breuer KS (2008) To slip or not to slip: water flows in hydrophilic and hydrophobic microchannels. *ASME Int Mech Eng Congr Expo Proc*:557–564. <https://doi.org/10.1115/IMECE2002-33707>
44. Zhou G, Yao SC (2011) Effect of surface roughness on laminar liquid flow in micro-channels. *Appl Therm Eng* 31:228–234. <https://doi.org/10.1016/j.applthermaleng.2010.09.002>
45. Alford TL, Feldman LC, Mayer JW (2007) Fundamentals of nanoscale film analysis. Springer, USA
46. Hwang Y, Paydar OH, Candler RN (2015) 3D printed molds for non-planar PDMS microfluidic channels. *Sensors Actuators, A Phys* 226:137–142. <https://doi.org/10.1016/j.sna.2015.02.028>
47. Villegas M, Cetinic Z, Shakeri A, Didar TF (2018) Fabricating smooth PDMS microfluidic channels from low-resolution 3D printed molds using an omniphobic lubricant-infused coating. *Anal Chim Acta* 1000:248–255. <https://doi.org/10.1016/j.aca.2017.11.063>
48. Vaidya N, Solgaard O (2018) 3D printed optics with nanometer scale surface roughness. *Microsystems Nanoeng* 4. <https://doi.org/10.1038/s41378-018-0015-4>
49. Weilin Q, Mohiuddin Mala G, Dongqing L (2000) Pressure-driven water flows in trapezoidal silicon microchannels. *Int J Heat Mass Transf* 43:353–364. [https://doi.org/10.1016/S0017-9310\(99\)00148-9](https://doi.org/10.1016/S0017-9310(99)00148-9)
50. Pfund R, Rector D, Shekarraz A et al (2000) Pressure drop measurements in a microchannel. *AIChE J* 46:1496–1507. <https://doi.org/10.1002/AIC.690460803>
51. Warr CA, Hinnen HS, Avery S et al (2021) 3D-printed microfluidic droplet generator with hydrophilic and hydrophobic polymers. *Micromachines* 12:1–13. <https://doi.org/10.3390/mi12010091>
52. Eduati F, Utharala R, Madhavan D et al (2018) A microfluidics platform for combinatorial drug screening on cancer biopsies. *Nat Commun* 9. <https://doi.org/10.1038/s41467-018-04919-w>
53. Song R, Abbasi MS, Lee J (2019) Fabrication of 3D printed modular microfluidic system for generating and manipulating complex

- emulsion droplets. *Microfluid Nanofluidics* 23:1–11. <https://doi.org/10.1007/s10404-019-2258-2>
54. Sun YS (2016) Comparison of chip inlet geometry in microfluidic devices for cell studies. *Molecules* 21. <https://doi.org/10.3390/molecules21060778>
55. Cennamo N, Saitta L, Tosto C et al (2021) Microstructured surface plasmon resonance sensor based on inkjet 3d printing using photocurable resins with tailored refractive index. *Polymers* 13. <https://doi.org/10.3390/polym13152518>

**Publisher's Note** Springer Nature remains neutral with regard to jurisdictional claims in published maps and institutional affiliations.